

Kármán vortex street in a spin-orbit-coupled Bose-Einstein condensate with PT symmetry

Kai-Hua Shao(邵凯花), Bao-Long Xi(席保龙), Zhong-Hong Xi(席忠红),Pu Tu(涂朴), Qing-Qing Wang(王青青), Jin-Ping Ma(马金萍),Xi Zhao(赵茜), and Yu-Ren Shi(石玉仁)

Citation: Chin. Phys. B, 2024, 33 (**6**): 060501. DOI:10.1088/1674-1056/ad2bf3
Journal homepage: http://cpb.iphy.ac.cn; http://iopscience.iop.org/cpb

What follows is a list of articles you may be interested in

Dynamics of bubble-shaped Bose-Einstein condensates on two-dimensional cross-section in micro-gravity environment

Tie-Fu Zhang(张铁夫), Cheng-Xi Li(李成蹊), and Wu-Ming Liu(刘伍明)
Chin. Phys. B, 2023, 32 (**9**): 090501. DOI: 10.1088/1674-1056/acd922

Merging and splitting dynamics between two bright solitons in dipolar Bose-Einstein condensates

Xin Li(李欣), Peng Gao(高鹏), Zhan-Ying Yang(杨战营), and Wen-Li Yang(杨文力)
Chin. Phys. B, 2021, 30 (**12**): 120501. DOI: 10.1088/1674-1056/abff3f

Solitons in nonlinear systems and eigen-states in quantum wells

Li-Chen Zhao(赵立臣), Zhan-Ying Yang(杨战营), Wen-Li Yang(杨文力)
Chin. Phys. B, 2019, 28 (**1**): 010501. DOI: 10.1088/1674-1056/28/1/010501

Domain walls and their interactions in a two-component Bose-Einstein condensate

Ling-Zheng Meng(孟令正), Yan-Hong Qin(秦艳红), Li-Chen Zhao(赵立臣), Zhan-Ying Yang(杨战营)
Chin. Phys. B, 2019, 28 (**6**): 060502. DOI: 10.1088/1674-1056/28/6/060502

Dynamics of spinor Bose-Einstein condensate subject to dissipation

Man-Man Pang(庞曼曼), Ya-Jiang Hao(郝亚江)
Chin. Phys. B, 2016, 25 (**4**): 040501. DOI: 10.1088/1674-1056/25/4/040501

Kármán vortex street in a spin–orbit-coupled Bose–Einstein condensate with PT symmetry

Kai-Hua Shao(邵凯花)[1], Bao-Long Xi(席保龙)[1], Zhong-Hong Xi(席忠红)[1,2], Pu Tu(涂朴)[1,3], Qing-Qing Wang(王青青)[1], Jin-Ping Ma(马金萍)[1], Xi Zhao(赵茜)[1], and Yu-Ren Shi(石玉仁)[1,†]

[1] *College of Physics and Electronic Engineering, Northwest Normal University, Lanzhou* 730070, *China*
[2] *College of Physics and Hydropower Engineering, Gansu Normal College For Nationalities, Hezuo* 747000, *China*
[3] *College of Intelligent Manufacturing, Sichuan University of Arts and Science, Dazhou* 635000, *China*

(Received 13 December 2023; revised manuscript received 13 February 2024; accepted manuscript online 22 February 2024)

The dynamics of spin–orbit-coupled Bose–Einstein condensate with parity-time symmetry through a moving obstacle potential is simulated numerically. In the miscible two-component condensate, the formation of the Kármán vortex street is observed in one component, while 'the half-quantum vortex street' is observed in the other component. Other patterns of vortex shedding, such as oblique vortex dipoles, V-shaped vortex pairs, irregular turbulence, and combined modes of various wakes, can also be found. The ratio of inter-vortex spacing in one row to the distance between vortex rows is approximately 0.18, which is less than the stability condition 0.28 of classical fluid. The drag force acting on the obstacle potential is simulated. The parametric regions of Kármán vortex street and other vortex patterns are calculated. The range of Kármán vortex street is surrounded by the region of combined modes. In addition, spin–orbit coupling disrupts the symmetry of the system and the gain-loss affects the local particle distribution of the system, which leads to the local symmetry breaking of the system, and finally influences the stability of the Kármán vortex street. Finally, we propose an experimental protocol to realize the Kármán vortex street in a system.

Keywords: Kármán vortex street, Bose–Einstein condensate, spin–orbit-coupled, parity-time symmetry

PACS: 05.30.Jp, 03.75.Mn, 03.75.Kk, 11.30.Er **DOI:** 10.1088/1674-1056/ad2bf3

1. Introduction

Bose–Einstein condensation (BEC) is a quantum phenomenon in which all atoms below a certain temperature are gathered in the lowest energy quantum state.[1] Since the BEC was first experimentally achieved in 1995,[2–4] it has provided a precisely regulated platform for studying superfluid phenomena. A variety of phenomena with moving obstacle potentials in the BEC have been investigated, such as generation of vortices in trapped system,[5] the Kármán vortex street,[5–7] three-dimensional dynamics[8,9] and so on. When the obstacle potential moves at appropriate conditions, vortices are created and alternately shed on either side of the obstacle, forming the Kármán vortex street.[10–13] This phenomenon is not only common in classical fluids but is also found in superfluids. In 2010, Sasaki *et al*. theoretically researched the Kármán vortex street in BEC. They illustrated that vortex pairs alternately arrange behind the obstacle potential.[7] Then, Saito *et al*. investigated dynamics of a superfluid flow through the obstacle,[14] the result shows that oscillation of the obstacle modulates the vortex street. Subsequently, Stagg *et al*. studied vortices generated after an oval obstacle.[15] In addition, Kármán vortex street has been reported in a two-component BEC.[16,17] Through a series of experiments, Kwon *et al*. reported vortices shedding from the obstacle potential by focusing a repulsive Gaussian laser beam which moves at a certain speed in a highly oblate BEC.[18–20]

In experiments, BEC with artificial spin–orbit coupled (SOC) has been achieved, which also provides a platform for exploring novel quantum phenomena. In 2011, the ^{87}Rb BEC with SOC was realized experimentally.[21] Then, the same protocol has been applied to realize SOC Fermi gases.[22,23] The experimental realization of SOC quantum gases has stimulated interest in quantum phase transitions,[24] topological excitations[25] and spintronic devices.[26] In addition, parity–time (PT) symmetry is another popular study area in physics.[27,28] In 1998, Bender and Boettcher put forward a non-Hermitian Hamiltonian with PT symmetry and they found that the energy spectrum of non-Hermitian operators remains completely real.[27] Meanwhile, the potential associated with PT symmetric Hamiltonian should satisfy an even function for the real part and an odd one for the imaginary part. Considering the condition of complex potential, PT symmetric Hamiltonian is employed to model, which aims to balance gain and loss. The gain can be accomplished by using an atom laser to inject atoms into the condensate.[29] The loss is achieved via exciting atoms to an excited state using a laser beam, they are then jetted out from the condensate by photon recoil.[30]

In recent years, SOC and PT symmetric systems have become research highlights in experimental and theoretical fields. One-dimensional and two-dimensional solitons of simulating SOC with PT symmetry have been investigated.[31]

[†]Corresponding author. E-mail: shiyr@nwnu.edu.cn

© 2024 Chinese Physical Society and IOP Publishing Ltd

By introducing imaginary potential, Zhang *et al*. theoretically studied energy band structures of one-dimensional non-Hermitian SOC Su–Schrieffer–Heeger model.[32] In 2022, Qin *et al*. showed that balancing gain and loss can compound an imaginary SOC in a pseudo-spin-1/2 system with PT symmetry.[33] As far as we know, there has been no experimental or theoretical research about Kármán vortex street in SOC BEC with PT symmetry. In particular, we want to know how SOC strength and gain-loss intensity affect the stability of the Kármán vortex street.

In this work, we investigate various wake patterns that vortices shed from the moving obstacle potential in SOC BEC with PT symmetry. The results indicate that vortex pairs arise behind the obstacle, forming all kinds of wakes. The frequency and magnitude of the drag force are different from the case of scalar BEC. In addition, we simulate vortex patterns systematically, which aims to determine the parameter region corresponding to various wakes. Finally, we propose an experimental protocol to realize Kármán vortex street in the SOC BEC with PT symmetry. The outline of this paper is as follows. In Section 2, we formulate theoretical model of the system. Section 3 shows the numerical results. Finally, we generalize the main results in Section 4.

2. Theoretical method

Within the mean-field approximation, we research the two-component SOC BEC with PT symmetry. The Hamiltonian of the system is given by[34,35]

$$H = \int \mathrm{d}\boldsymbol{r}\boldsymbol{\Psi}^{\dagger}\left(\frac{\boldsymbol{p}^2}{2m}+V-\frac{\hbar k_0}{m}\boldsymbol{p}\cdot\boldsymbol{\sigma}_{\perp}\right)\boldsymbol{\Psi} + \int \mathrm{d}\boldsymbol{r}\left(\sum_{j=\uparrow,\downarrow}\frac{g_{jj}}{2}|\psi_j|^4+g_{\uparrow\downarrow}|\psi_{\uparrow}|^2|\psi_{\downarrow}|^2\right), \quad (1)$$

where the wave function $\boldsymbol{\Psi}(\boldsymbol{r})=[\psi_{\uparrow}(\boldsymbol{r}),\psi_{\downarrow}(\boldsymbol{r})]^{\mathrm{T}}$ with T and $\boldsymbol{r}$ denote the transpose and Cartesian coordinate. m is the atomic mass, k_0 indicates the SOC strength, and $\boldsymbol{\sigma}_{\perp}=(\sigma_x,\sigma_y)$ are the 2×2 Pauli matrices. g_{jj} and g_{jl} play the roles of the intra- and intercomponent interaction coefficients, respectively. $g_{jl}=4\pi\hbar^2 a_{jl}/m$, here $a_{jl}(a_{jl}=a_{\uparrow\downarrow})$ are the s-wave scattering lengths. In experiments, BEC is usually confined in a harmonic potential $V_{\mathrm{har}}=\frac{1}{2}m(\omega_x^2x^2+\omega_y^2y^2+\omega_z^2z^2)$, where ω_x, ω_y, ω_z denote the trapping potential frequencies along x, y, z directions, respectively.

In the following, we assume that the restrain along z direction is stronger than any other, the energy scale of $\hbar\omega_z$ is much larger than $\hbar\omega_x$ and $\hbar\omega_y$.[36–38] Thus, the system is reduced to quasi-two-dimensional. Then the wave function is rationally expressed as $\psi_j(\boldsymbol{r},t)=\varphi(x,y,t)\phi_{j0}(z)\,\mathrm{e}^{-\mathrm{i}\omega_z t/2}$, and the movement of atoms along the z direction is frozen into the ground state $\phi_{j0}(z)=(m_j\omega_z/(\pi\hbar))^{1/4}\,\mathrm{e}^{-m_j\omega_z z^2/2\hbar}$. Furthermore, the various variables are normalized by $\tilde{t}=\omega_0 t$, $\tilde{x}=x/a_{h0}$, $\tilde{y}=y/a_{h0}$, $\tilde{\psi}_j=\psi_j(x,y,t)/\sqrt{n_0/a_{h0}^2}$, $\tilde{g}_{jl}=4\pi n_0 a_{jl}/(\sqrt{2\pi}l_z)$, with $\omega_0=\min(\omega_x,\omega_y)$, $l_z=\sqrt{\hbar/(m\omega_z)}$ and $a_{h0}=\sqrt{\hbar/(m\omega_0)}$, where n_0 represents the characteristic particle number density. The total particles are $N=n_0\int|\boldsymbol{\Psi}|^2\mathrm{d}x\mathrm{d}y$. For convenience, the "$\sim$" on all variables are omitted. One can obtain the dimensionless quasi-two-dimensional Gross–Pitaevskii (GP) equation as

$$\begin{aligned}
\mathrm{i}\frac{\partial\psi_{\uparrow}}{\partial t} &= \left[-\frac{1}{2}\nabla^2+V+g_{\uparrow\uparrow}|\psi_{\uparrow}|^2+g_{\uparrow\downarrow}|\psi_{\downarrow}|^2\right]\psi_{\uparrow} \\
&\quad +\mathrm{i}\kappa\partial_-\psi_{\downarrow}, \\
\mathrm{i}\frac{\partial\psi_{\downarrow}}{\partial t} &= \left[-\frac{1}{2}\nabla^2+V+g_{\downarrow\uparrow}|\psi_{\uparrow}|^2+g_{\downarrow\downarrow}|\psi_{\downarrow}|^2\right]\psi_{\downarrow} \\
&\quad +\mathrm{i}\kappa\partial_+\psi_{\uparrow}, \qquad (2)
\end{aligned}$$

where $\kappa=k_0\sqrt{m/(\hbar^3\omega_0)}$, $\partial_{\pm}=\partial/\partial x\pm\mathrm{i}\partial/\partial y$. ∇^2 is the two-dimensional Laplacian operator. $\psi_{\uparrow}$ and $\psi_{\downarrow}$ indicate component 1 and 2, respectively.

The initial state is applied to the ground state, which is obtained by the imaginary-time propagation method with a zero potential velocity. The initial condition $\psi_{\uparrow}=\psi_{\downarrow}=1$ is employed. The interaction parameters are adopted as $g_{\uparrow\uparrow}=g_{\downarrow\downarrow}=1$ and $g_{\uparrow\downarrow}=g_{\downarrow\uparrow}=0.3$, which satisfy $g_{\uparrow\uparrow}g_{\downarrow\downarrow}>g_{\uparrow\downarrow}^2$, thus the two components are miscible.[39] A small amount of disturbance is added to break the symmetry of system. Then, Eq. (2) will be numerically solved by the time-splitting Fourier pseudo-spectral method under periodic boundary conditions.[40] The numerical domain is chosen as $[-256,256]\otimes[-64,64]$ and discretized uniformly into 2048×512 grids.

3. Numerical results

In the present work, an external potential $V=V_{\mathrm{R}}+\mathrm{i}V_{\mathrm{I}}$ is employed, which satisfies PT symmetry. That is, the Gaussian obstacle potential V_{R} is an even function while the imaginary part V_{I} should be an odd one. The Gaussian obstacle potential moves with a certain velocity υ, which is expressed as[7]

$$V_{\mathrm{R}} = V_0\left[\mathrm{e}^{-\frac{(x-x_{0\mathrm{r}}+\upsilon t)^2+(y+y_{0\mathrm{r}})^2}{d^2}}+\mathrm{e}^{-\frac{(x+x_{0\mathrm{r}}-\upsilon t)^2+(y-y_{0\mathrm{r}})^2}{d^2}}\right], \quad (3)$$

where $(\pm x_{0\mathrm{r}},\pm y_{0\mathrm{r}})$ is the center position of V_{R} at $t=0$. V_0 is the peak strength and d represents width of obstacle potential. V_{R} is generated by a repulsive Gaussian laser beam in experiments.[18,19,41] Then, the imaginary part of external potential is adopted as[42]

$$V_{\mathrm{I}}=\Gamma\left[\mathrm{e}^{-\frac{(x-x_{0\mathrm{i}})^2+(y+y_{0\mathrm{i}})^2}{d^2}}-\mathrm{e}^{-\frac{(x+x_{0\mathrm{i}})^2+(y-y_{0\mathrm{i}})^2}{d^2}}\right]. \quad (4)$$

The center position of V_{I} is fixed at $(\pm x_{0\mathrm{i}},\pm y_{0\mathrm{i}})$ when performing the nonlinear dynamical evolution. It acts as additional gain around $(x_{0\mathrm{i}},-y_{0\mathrm{i}})=(0,-70)$ or loss near $(x_{0\mathrm{i}},y_{0\mathrm{i}})=(0,70)$. But the total particles are still conserved. Γ is the gain-loss intensity and d denotes the width that is the same as the Gaussian obstacle potential.

In order to study the various wakes, we consider that the Gaussian obstacle potential $V_{\rm R}$ moves from $(x_{0\rm r}, y_{0\rm r}) = (409.6, 60)$ along $-x$ direction with $V_0 = 100$, while another moves from $(-x_{0\rm r}, -y_{0\rm r}) = (-409.6, -60)$ along x direction with the same peak intensity. Vortex shedding patterns are studied by adjusting the velocity and width of the obstacle potential at the SOC strength $\kappa = 0.01$ and the gain-loss intensity $\Gamma = 0.02$.

Figure 1 indicates the density and phase distributions of oblique vortex dipoles and V-shaped vortex pairs. Because wakes in the miscible two-component of SOC BEC with PT symmetry are similar, density $|\psi_\downarrow|$ and phase $\arg|\psi_\downarrow|$ distributions are omitted. However, we can observe the distribution of vortex pairs in component 2 (shown in red). That is, the atoms in component 1 fill into the central position of the vortex in component 2, but this position is without fill. Thus, the vortex center in component 2 changes into the density peak of vortex in component 1. The composite structure emerging from two components is called 'the coreless vortex';[43] that is, changed with the velocity and width of the obstacle potential. In Fig. 1(a), it is obvious that vortex pairs formed by the point vortex are obliquely drift and their centers are clearly not in the same straight line. A pair of point vortices have opposite circulation $\pm 2\pi\hbar/m$, which corresponds to dimensionless quantity $\pm 2\pi$. The distance between two point vortices changes slightly with the movement of obstacle potential. In addition, we note that the vortex pairs in component 2 are more than those in component 1. This is owing to that SOC breaks the symmetry and the gain-loss intensity Γ causes the distribution of atoms to be uneven in the system. When the velocity of obstacle has suitable values, vortex pairs will shed alternately (see Fig. 1(b)). The rotation direction of vortex–antivortex pairs is the same as the situation shown in Fig. 1(a). The vortex–antivortex pairs drift along the $+y$ or $-y$ direction that V-shaped vortex pairs are formed. This phenomenon is understood as follows: vortex pairs will shed from obstacle potential when their velocity of movement exceeds a critical value. The critical velocity varies with the width and velocity of the obstacle potential. After vortex pairs are emitted from the obstacle, velocity of the vortices balances the main velocity field, which leads to the velocity around the obstacle being less than the critical velocity. Then, the vortex gradually moves away from the obstacle, until the main velocity exceeds the critical velocity again, which causes a new vortex pair to be generated.[44] When vortex pairs are properly disturbed, vortex pairs are unstable. Therefore, vortex pairs drift along the $+y$ or $-y$ direction.

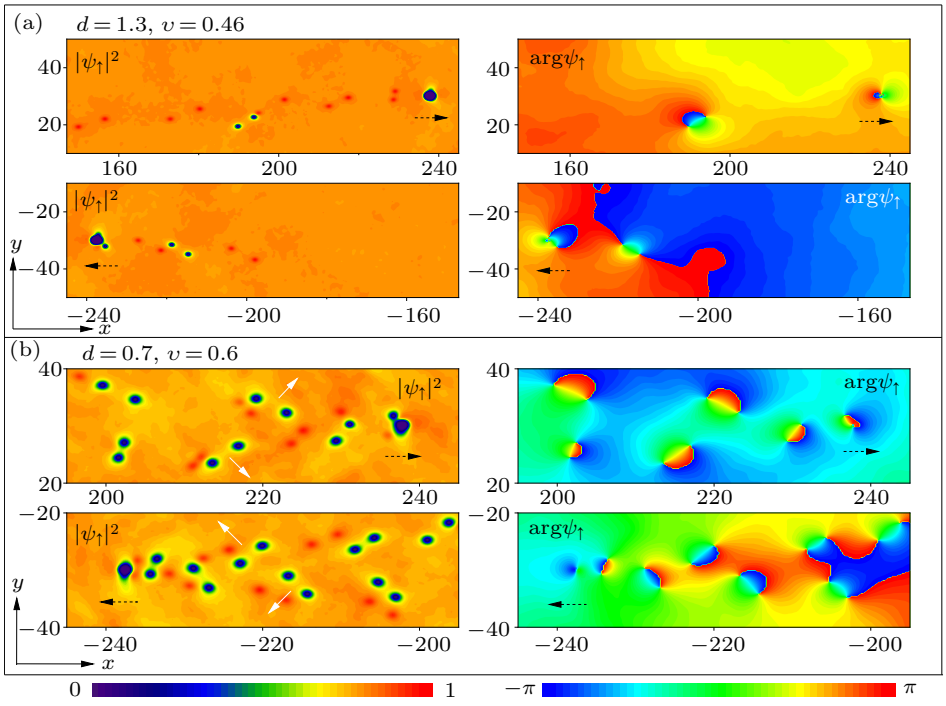


Fig. 1. Density $|\psi_\uparrow|^2$ and phase $\arg\psi_\uparrow$ distributions of the condensate. The velocity and width of obstacle potential are $d = 1.3, \upsilon = 0.46$ in (a) and $d = 0.7, \upsilon = 0.6$ in (b). The black-dotted arrows show the direction of the obstacle potential moves. The white arrows indicate the direction that the vortex pairs move.

Figure 2 plots the density and phase distributions of Kármán vortex street and irregular turbulence. In Fig. 2(a), periodic vortex pairs with opposite circulations are shed alternately from the obstacle potential, forming the Kármán vortex street. In component 2, the vortices are filled with particles from component 1 to form density peaks. It also forms

a wake pattern similar to the Kármán vortex street, which is called "the coreless vortex street". Two point vortices of the vortex pair have the same circulation. The angular frequency is $2\hbar/(mD^2)$.[45] Here D represents the distance between the two point vortices. It is found that the circulation of the upper row is $+2\pi$, while the lower row is -2π, as shown in the phase distributions of Fig. 2(a). The average dimensionless distance between the two rows of vortices is $b \approx 19.74$ and the inter-vortex spacing in one row is $l \approx 111.73$, which leads to $b/l \approx 0.18$. This result falls into the stability condition of Kármán vortex street $0.12 < b/l < 0.4$. It can be seen from Fig. 2(b) that the wake pattern is the irregular turbulence when we take $d = 2.8$, $\upsilon = 0.44$. It is obvious that the wake pattern has no apparent periodicity.

There are also various combined modes in the system. Figure 3 indicates some typical combined modes of vortex shedding from the obstacle potential which moves at various width and velocity. Figure 3(a) shows the combined mode of no vortex and oblique vortex dipoles. When the obstacle potential moves along x direction, the obstacle is surrounded by a stable laminar flow and no vortex is generated. Nevertheless, we find that the vortex dipoles are obliquely drifting when the obstacle moves along $-x$ direction. One can see from Fig. 3(b) that the vortex dipoles shed at different times in components 1 and 2. The vortex dipoles obliquely upward drift in component 1 while vortex dipoles evolve into V-shaped vortex pairs in component 2 as the obstacle potential moves along $-x$ direction. When it moves in the opposite direction, the V-shaped vortex pairs are formed in two components. The circulation of a single point vortex is consistent with Fig. 1(b). In Fig. 3(c), the Kármán vortex street and irregular turbulence have also formed behind the obstacle when the width d and velocity υ are fixed to 2.3 and 0.44. It is worth noting that the position of point vortices in component 1 is different from component 2 when the Kármán vortex street exists in the system. Here the circulation of vortex pairs in the upper row is -2π and the lower row is $+2\pi$. We have also measured the distance between two vortex rows being $b \approx 18.64$ and between two vortex pairs in the one vortex row being $l \approx 88.19$ on average. Thus, the ratio $b/l \approx 0.21$ is within the range of stability conditions. The combined modes are asymmetric because the local symmetry of the system has been broken by the SOC and imaginary part of external potential. The density distribution of particles is uneven in the system.

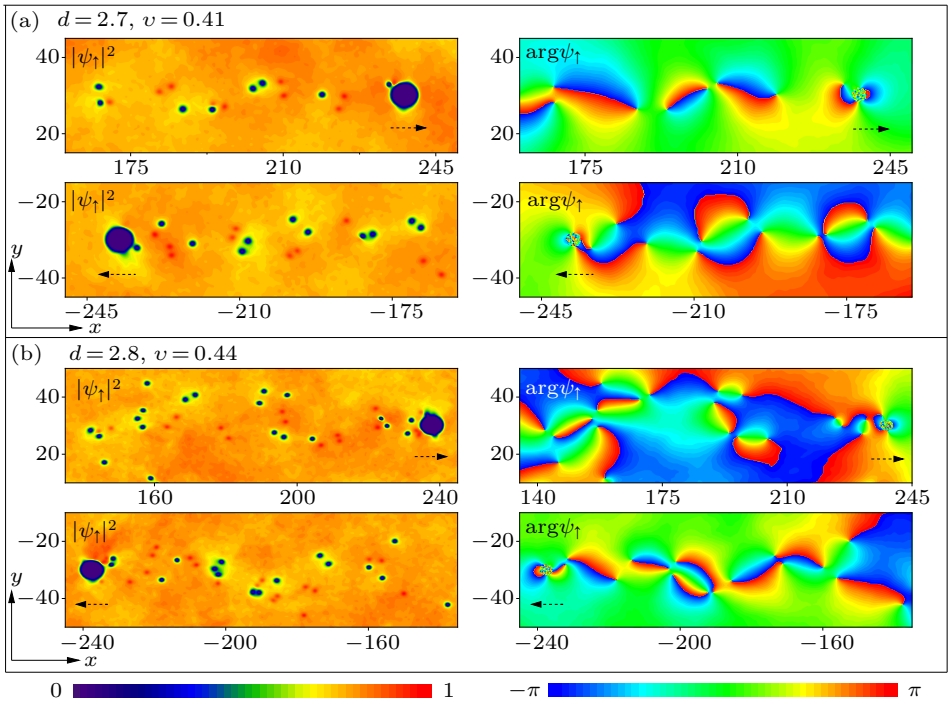


Fig. 2. Density $|\psi_\uparrow|^2$ and phase $\arg\psi_\uparrow$ distributions of the condensate. The velocity and width of obstacle potential are $d = 2.7, \upsilon = 0.41$ in (a) and $d = 2.8, \upsilon = 0.44$ in (b). The black dotted arrows show the direction of the obstacle potential moves.

The dimensionless drag force acting upon the obstacle potential of movement is defined as $\boldsymbol{f} = (f_x, f_y) = \mathrm{i}\partial_t \int (\boldsymbol{\Psi}^\dagger \nabla \boldsymbol{\Psi}) \mathrm{d}x\mathrm{d}y$. Here, $\boldsymbol{\Psi} = (\psi_\uparrow, \psi_\downarrow)^{\mathrm{T}}$ with T stands for transpose. Figures 4(a)–4(c) exhibit drag force corresponding to the Kármán vortex street displayed in Fig. 2(a). f_x expresses the shedding frequency of the vortex pair and f_y indicates the frequency of upward or downward motion of the vortex pair. One can notice that the crest value in Fig. 4(a) corresponds to the valley value in Fig. 4(b). This means that vortex pairs in component 1 and component 2 alternately shed

from the obstacle potential. It can be seen from Fig. 4(c) that $F_1 + F_2$ denotes the drag force described by two components. We find that f_x oscillates, but f_y is approximately zero for $t \lesssim 350\omega_0^{-1}$. This indicates that the vortex pair is shed symmetrically from the obstacle potential. Then, f_y oscillates periodically. Figures 4(d)–4(f) display the drag force corresponding to the combined mode of irregular turbulence and Kármán vortex street (see in Fig. 3(c)). Same as Figs. 4(a) and 4(b), the crest value in Fig. 4(d) corresponds to the valley value in Fig. 4(e). It is apparent that the oscillations of f_x and f_y become smaller than Figs. 4(a) and 4(b). In addition, the periodicity of f_y is not obvious compared to Fig. 4(c). Unlike the scalar BEC,[7] f_y oscillates almost from $t = 0$ in Fig. 4, indicating that the shedding vortex pair begins to drift from $t = 0$.

Figure 5 displays the parametric region of vortex shedding patterns with various d and υ. These patterns are classified as no vortex, oblique vortex dipoles, V-shaped vortex pairs, Kármán vortex street, irregular turbulence, and combined modes. The region of Kármán vortex street (see in Fig. 2(a)) is $1.1 < d < 3.2$ and $0.39 < \upsilon < 0.54$. Its range is rather restricted than other wake patterns. In addition, the area of Kármán vortex street is surrounded by the combined modes. The white curve indicates the fitting curve of dimensionless critical velocity $\upsilon_c/\upsilon_s = c(1/d)^p$, here $c \approx 1/2.11$ and $p \approx 1/3.43$, which is consistent with the experimental results obtained in the highly oblate BEC system.[19] $\upsilon_s = \sqrt{\hbar\omega_x/m}$ is the speed of sound. The critical velocity υ_c relies on the velocity and width of the obstacle potential.

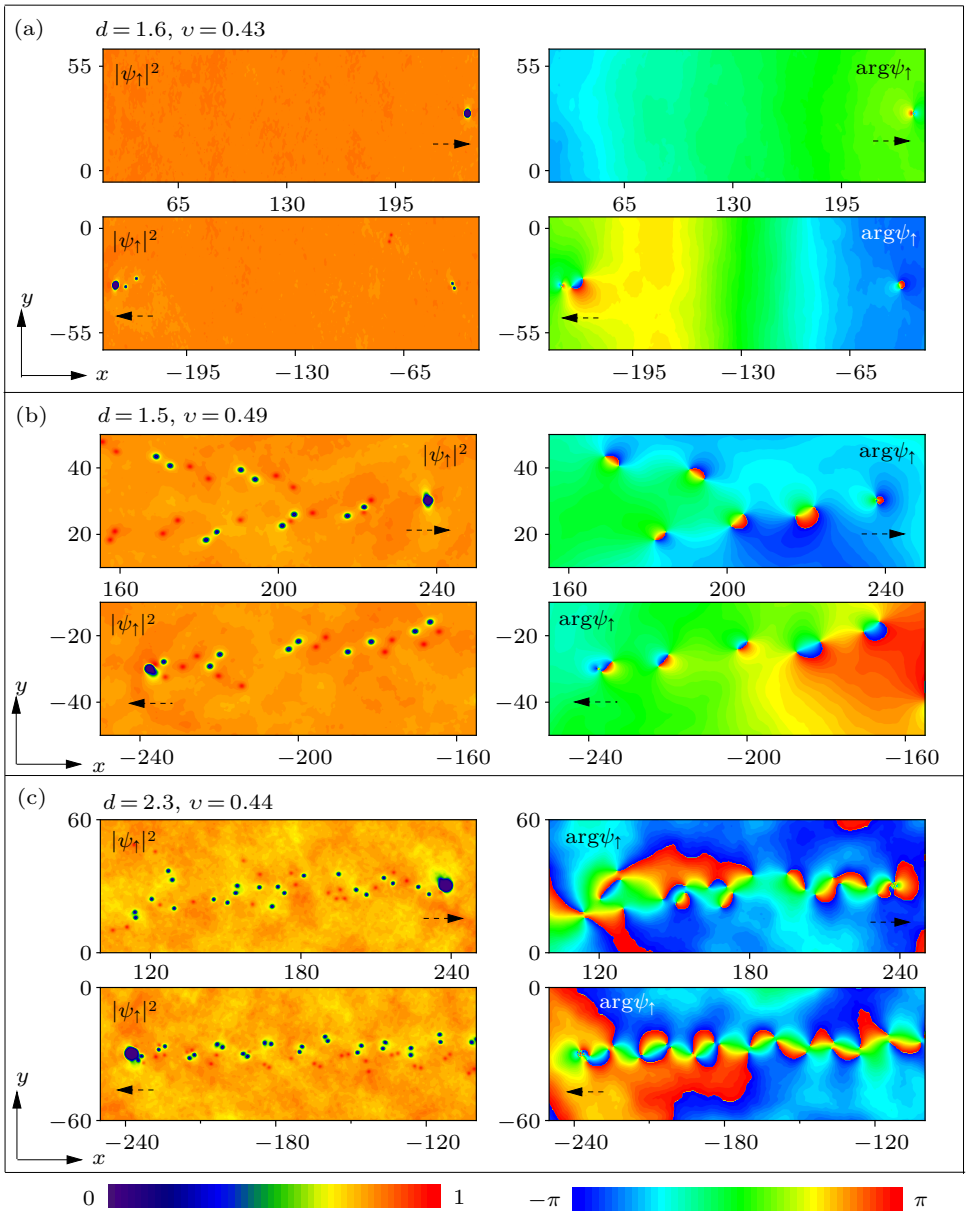


Fig. 3. Density $|\psi_\uparrow|^2$ and phase $\arg\psi_\uparrow$ distributions of the condensate. The velocity and width of obstacle potential are $d = 1.6, \upsilon = 0.43$ in (a), $d = 1.5, \upsilon = 0.49$ in (b) and $d = 2.3, \upsilon = 0.44$ in (c). The black dotted arrows show the direction of the obstacle potential moves.

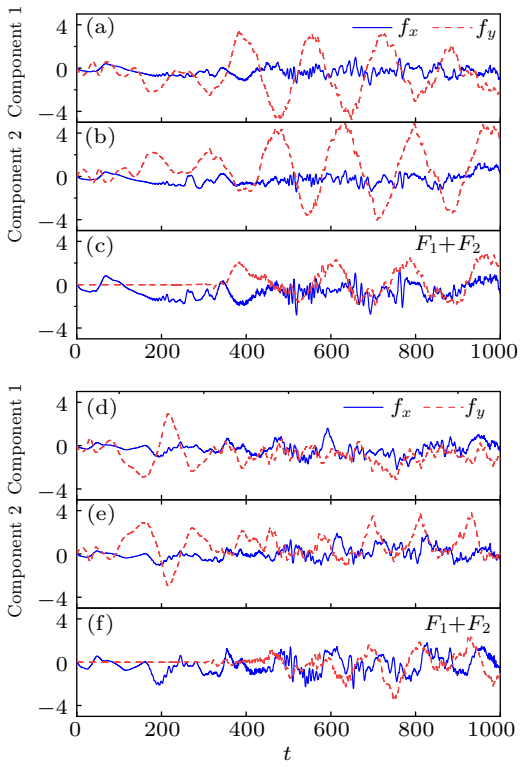


Fig. 4. The variation of the drag force over time. The blue-solid line and the red-dashed line correspond to f_x and f_y, respectively. The parameters are consistent with those in Figs. 2(a) and 3(c). F_1+F_1 denotes the state described by $\psi_\uparrow+\psi_\downarrow$.

In order to research the dynamics behavior of Kármán vortex street formation that is affected by the imaginary part of external potential with gain and loss, Fig. 6 exhibits the dynamics process of Kármán vortex street in the system. In the previous stage, the moving obstacle potential does not arrive at the position of the imaginary part. That is, the vortex pairs that shed behind the obstacle potential are almost unaffected by the imaginary part. During this period, vortex pairs form the Kármán vortex street, as shown in Figs. 6(a) and 6(b). As time goes on, the obstacle enters and then passes the region of the imaginary part. It affects the distribution of particles, leading to track of vortices change in the wake (see in Figs. 6(c) and 6(d)). Gain-loss intensity has less influence on vortices when the obstacle moves away from the position of the imaginary part. Vortex pairs with opposite circulations are re-released alternately from obstacle potential, forming Kármán vortex street, as shown in Figs. 6(e) and 6(f)). It is obvious that paroxysmal vortex street appears in the system.

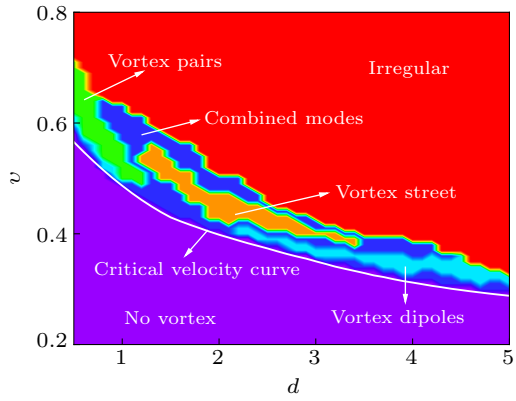


Fig. 5. Dependence of the various vortex patterns on the width d and velocity v of moving obstacle potential. The purple area is consistent with the stable laminar flow. The light blue, green, orange, red, and blue areas correspond to the wake patterns shown in Figs. 1(a), 1(b), 2(a), 2(b), and 3. The white curve is the fitting curve of dimensionless critical velocity for vortex emission.

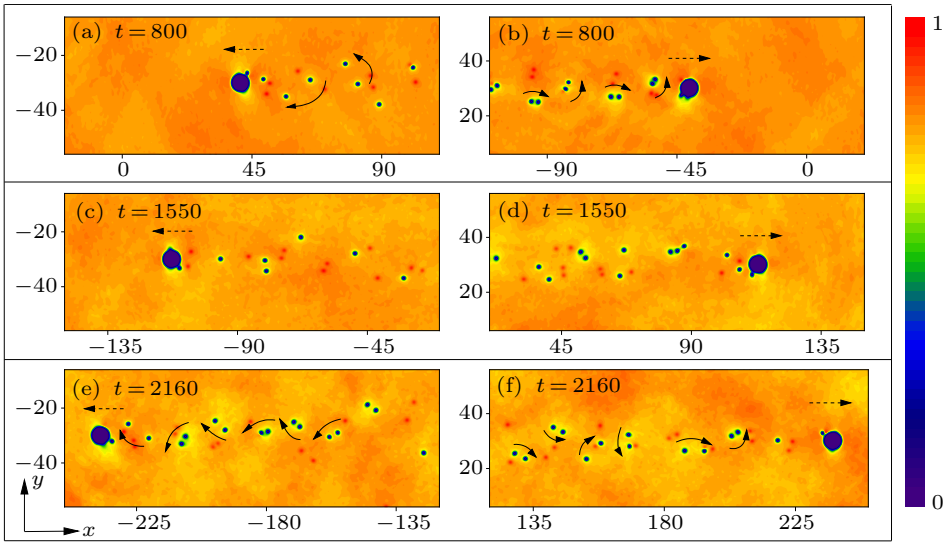


Fig. 6. Dynamics process of the Kármán vortex street formation behind the obstacle potential for the parameter in Fig. 2(a). The black-dotted arrows show the direction of the moving obstacle potential. The solid curved arrows indicate the direction of rotation of vortex pairs. (a) and (b) $t=800$, (c) and (d) $t=1550$, (e) and (f) $t=2160$.

Figure 7 shows more details of the dynamic evolutions of wake patterns with various the SOC strength κ and the gain-loss intensity Γ. Because the wake patterns in the two components are similar, density $|\psi_\downarrow|$ distributions are omitted. Here only the density $|\psi_\uparrow|$ distributions are considered. For $\kappa=0.01$ and $\Gamma=0.02$, stable Kármán vortex streets can eventually exist behind the obstacle potential in Fig. 7(a). One can see from Figs. 7(b) and 7(c) that irregular turbulence is

formed when κ increases to 0.02 and 0.04. It is obvious that increasing κ affects the distribution of vortex pairs. We also take into account the effect of Γ. As shown in Figs. 7(d)–7(f), Kármán vortex street will still form behind the obstacle as Γ increases. However, we note that the distance between a pair of point vortices varies. In Fig. 7(e), the distances clearly enlarge between two point vortices compared with Fig. 7(a) when the obstacle potential moves along $-x$ direction. Thus, both κ and Γ have an impact on the distributions of the point vortex and the stability of Kármán vortex street.

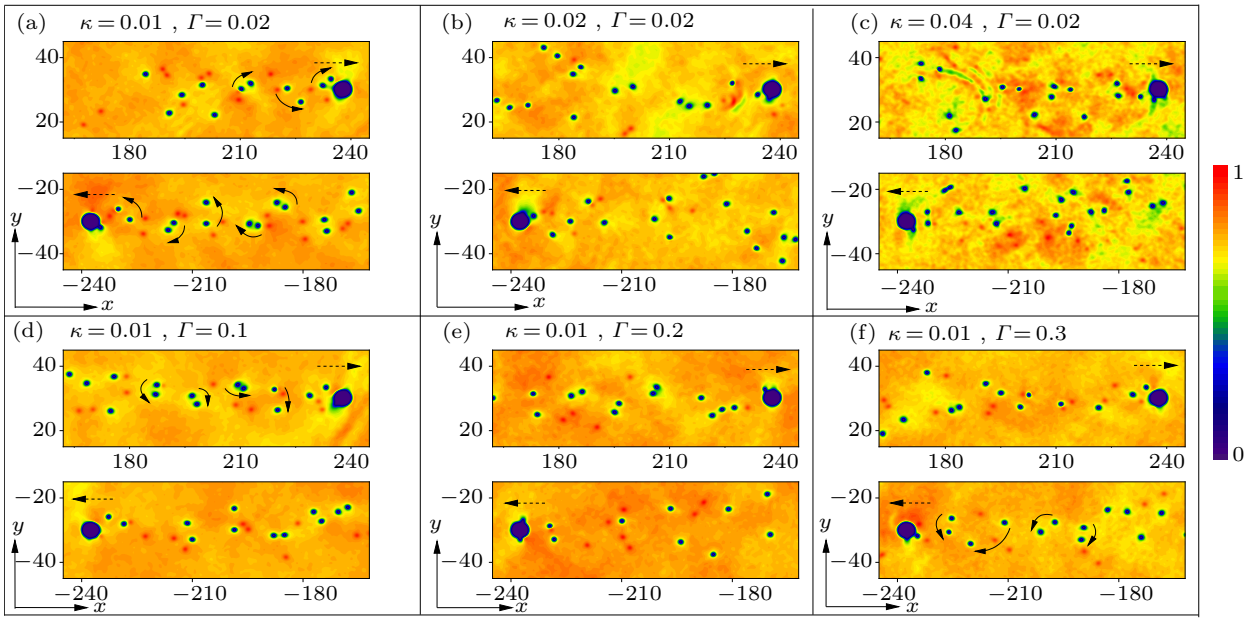


Fig. 7. Density distributions of condensates at width $d = 2.1$, velocity $\upsilon = 0.44$ with different SOC strength κ and the gain-loss intensity Γ. The black-dotted arrows show the direction of the moving obstacle potential.

To study Kármán vortex street in SOC BEC with PT symmetry, we propose a way that may be implemented experimentally. We consider ^{87}Rb in up and down hyperfine states: $|\uparrow\rangle = |f = 1, m_f = 0\rangle$ and $|\downarrow\rangle = |f = 1, m_f = -1\rangle$[21] with $m_1 = m_2 = 1.45 \times 10^{-25}$ kg. The number of atoms is $N \approx 2.62 \times 10^7$ ($n_0 = 100$) in condensate, which is confined in a harmonic potential with $(\omega_x, \omega_y, \omega_z) = 2\pi \times (32, 37, 100)$ Hz.[46] Thus, $\omega_0 = 2\pi \times 32$ Hz. The oscillator length is $a_{h0} = \sqrt{\hbar/m\omega_x} \approx 4.76$ μm. The s-wave scattering lengths are adjusted to $a_{\uparrow\uparrow} = a_{\downarrow\downarrow} \approx 100.86 a_{\rm B}$ and $a_{\uparrow\downarrow} = a_{\downarrow\uparrow} \approx 110.4 a_{\rm B}$,[47] here $a_{\rm B}$ is the Bohr radius. The interaction parameters are $g_{\uparrow\uparrow} = g_{\downarrow\downarrow} \approx 3.93 \times 10^{-51}$ J and $g_{\uparrow\downarrow} = g_{\downarrow\uparrow} \approx 4.83 \times 10^{-51}$ J, which correspond to dimensionless quantity $g_{\uparrow\uparrow} = g_{\downarrow\downarrow} = 1$ and $g_{\uparrow\downarrow} = g_{\downarrow\uparrow} = 0.3$ in Eq. (2). The Gaussian obstacle potential is generated by a repulsive Gaussian laser beam, which axially penetrates the condensate by two laser beams fixed in a laboratory frame.[18,19,48,49] The obstacle position is controlled by steering the laser beam with a piezo-driven mirror.[41] Then, by applying a triangular waveform to the acousto-optic deflector, the two Gaussian laser beams sweep from the initial position $(x_0, y_0) = (1.89, 0.27)$ mm along the $-x$ direction and from $(x_0, y_0) = (-1.89, -0.27)$ mm along the x direction at constant velocity $\upsilon = 0.062$ mm·s^{-1}, which corresponding to the parameters used in Fig. 2(a). The repulsive optical dipole force expels the atoms from the region of the highest laser intensity and forms a cylindrical hole. The laser power controls the size of its aperture. When the laser power is 3.6 μW, a cylindrical hole with a diameter of $d = 0.12$ μm is formed inside the condensate,[48] which corresponds to dimensionless quantities $d = 2.7$. The peak intensity of the obstacle potential is $V_0 = 3.36 \times 10^{-31}$ J. The imaginary part of the PT symmetric potential represents the gain-loss of atomic number. The gain is achieved by injecting atoms into the condensate using an atomic laser.[29] The loss is realized by using a laser beam to excite the atoms to an excited state and then eject them from the condensate by photon recoil.[30] The gain-loss intensity is $\Gamma = 6.72 \times 10^{-35}$ J, which corresponds to dimensionless quantities $\Gamma = 0.02$. Under these conditions, the Kármán vortex street shown in Fig. 2(a) may be realized.

4. Conclusion

In summary, we simulated and analyzed various wake patterns of the vortex shedding from the moving obstacle potential in a miscible two-component SOC BEC with PT symmetry. Oblique vortex dipoles, V-shaped vortex pair, irregular turbulence, and combined modes are observed. In particular, we also found Kármán vortex street, and its stability is affected by the SOC strength and the gain-loss intensity. Numerical results indicate that the wake pattern evolves from steady laminar flow to irregular turbulence with increasing velocity when the width of obstacle potential is given. We calculated b/l, which is lower than the stability criterion 0.28 in clas-

sical fluid. Meanwhile, the drag force acting on the obstacle potential is calculated. The results show that the frequency and magnitude of the drag force are different from those of the scalar BEC without SOC and PT symmetry. The parametric regions in which various vortex patterns emerge are presented. Finally, we proposed a practical solution to realize the Kármán vortex street in experiment.

Acknowledgement

Project supported by the National Natural Science Foundation of China (Grant Nos. 12065022 and 12147213).

References

[1] Bose V 1924 *Zeitschrift fur Physik* **26** 178
[2] Anderson M H, Ensher J R, Matthews M R, Wieman C E and Cornell E A 1995 *Science* **269** 198
[3] Edwards M, Dodd R J, Clark C W, Ruprecht P A and Burnett K 1996 *Phys. Rev. A* **53** R1950
[4] Davis K B, Mewes M O, Andrews M R, van Druten N J, Durfee D S, Kurn D M and Ketterle W 1995 *Phys. Rev. Lett.* **75** 3969
[5] Jackson B, McCann J F and Adams C S 1998 *Phys. Rev. Lett.* **80** 3903
[6] Reeves M T, Billam T P, Anderson B P and Bradley A S 2015 *Phys. Rev. Lett.* **114** 155302
[7] Sasaki K, Suzuki N and Saito H 2010 *Phys. Rev. Lett.* **104** 150404
[8] Nore C, Huepe C and Brachet M E 2000 *Phys. Rev. Lett.* **84** 2191
[9] Aftalion A, Du Q and Pomeau Y 2003 *Phys. Rev. Lett.* **91** 090407
[10] Kim I and Wu X L 2015 *Phys. Rev. E* **92** 043011
[11] Crowdy D G and Krishnamurthy V S 2017 *Phys. Rev. Fluids* **2** 114701
[12] Iiman M 2019 *Phys. Rev. E* **99** 062203
[13] Boniface P, Lebon L, Limat L and Receveur M 2017 *Europhys. Lett.* **117** 34001
[14] Saito H, Tazaki K and Aioi T 2013 *Europhys. Lett.* **9** 121
[15] Stagg G W, Parker N G and Barenghi C F 2014 *J. Phys. B: Atom. Mol. Opt. Phys.* **47** 095304
[16] Ancilotto F, Barranco M, Eloranta J and Pi M 2017 *Phys. Rev. B* **96** 064503
[17] Wang J, Li X L, Ren X P, Fan X B, Zhou Y S, Meng H J, Wan X H, Zhang J, Shao K H and Shi Y R 2022 *Euro. Phys. J. Plus* **137** 1216
[18] Kwon W J, Moon G, Choi J Y, Seo S W and Shin Y 2014 *Phys. Rev. A* **90** 063627
[19] Kwon W J, Moon G, Choi J Y, Seo S W and Shin Y 2015 *Phys. Rev. A* **91** 053615
[20] Kwon W J, Seo S W and Shin Y 2015 *Phys. Rev. A* **92** 033613
[21] Lin Y J, García K J and Spielman I B 2011 *Nature* **471** 83
[22] Wang P J, Yu Z Q, Fu Z K, Miao J, Huang L H, Chai S J, Zhai H and Zhang J 2012 *Phys. Rev. Lett.* **109** 095301
[23] Cheuk L W, Sommer A T, Hadzibabic Z, Yefsah T, Bakr W S and Zwierlein M W 2012 *Phys. Rev. Lett.* **109** 095302
[24] Cabedo J and Celi A 2021 *Phys. Rev. Res* **23** 043215
[25] Gong M, Tewari S and Zhang C 2011 *Phys. Rev. Lett.* **107** 195303
[26] Koralek J D, Weber C P, Orenstein J, Bernevig B A, Zhang S C, Mack S and Awschalom D D 2009 *Nature* **458** 7238
[27] Bender C M 2007 *Reports on Progress in Physics* **70** 947
[28] El-Ganainy R, Makris K G, Khajavikhan M, Musslimani Z H, Rotter S and Christodoulides D N 2018 *Nat. Phys.* **14** 11
[29] Robins N P, Figl C, Jeppesen M, Dennis G R and Close J D 2008 *Nat. Phys.* **4** 731
[30] Li J, Harter A K, Liu J, Melo L, Joglekar Y N and Luo L 2019 *Nat. Commun.* **10** 855
[31] Sakaguchi H and Malomed B A 2016 *New J. Phys.* **18** 105005
[32] Li J R, Wang Z A and Zhang L L 2023 *Annals of Physics* **448** 169165
[33] Qin J L, Zhou L and Dong G J 2022 *New J. Phys.* **24** 063025
[34] Kato M, Zhang X F and Saito H 2017 *Phys. Rev. A* **95** 043605
[35] Cui X L 2022 *Phys. Rev. Res.* **4** 013047
[36] Wang L X, Dai C Q, Wen L, Liu T, Jiang H F, Saito H, Zhang S G and Zhang X F 2018 *Phys. Rev. A* **97** 063607
[37] Zhang X F, Du Z J, Tan R B, Dong R F, Chang H and Zhang S G 2014 *Annals of Physics* **346** 154
[38] Wang D S, Song S W, Xiong B and Liu W M 2011 *Phys. Rev. A* **84** 053607
[39] Ishino S, Tsubota M and Takeuchi H 2013 *Phys. Rev. A* **88** 063617
[40] Bao W Z, Chern I L and Lim F Y 2006 *Journal of Computational Physics* **219** 836
[41] Kwon W J, Kim J H, Seo S W and Shin Y 2016 *Phys. Rev. Lett.* **117** 245301
[42] Schwarz L, Cartarius H, Musslimani Z H, Main J and Wunner G 2017 *Phys. Rev. A* **95** 053613
[43] Seo S W, Kwon W J, Kang S and Shin Y 2016 *Phys. Rev. Lett.* **116** 185301
[44] Frisch T, Pomeau Y and Rica S 1992 *Phys. Rev. Lett.* **69** 1644
[45] Fujiyama S and Tsubota M 2009 *Phys. Rev. B* **79** 094513
[46] Jiménez-García K, LeBlanc L J, Williams R A, Beeler M C, Qu C, Gong M, Zhang C and Spielman I B 2015 *Phys. Rev. Lett.* **114** 125301
[47] Lin Z 2020 *Ann. Phys.* **533** 1
[48] Raman C, Köhl M, Onofrio R, Durfee D S, Kuklewicz C E, Hadzibabic Z and Ketterle W 1999 *Phys. Rev. Lett.* **83** 2502
[49] Neely T W, Samson E C, Bradley A S, Davis M J and Anderson B P 2010 *Phys. Rev. Lett.* **104** 160401